COMPUTATIONAL AEROTHERMODYNAMICS IN AEROASSIST APPLICATIONS

Peter A. Gnoffo[†]
p.a.gnoffo@larc.nasa.gov
NASA Langley Research Center
Hampton, VA 23681-0001

Abstract

Aeroassisted planetary entry uses atmospheric drag to decelerate spacecraft from super-orbital to orbital or sub-orbital velocities. Numerical simulation of flow fields surrounding these spacecraft during hypersonic atmospheric entry is required to define aerothermal loads. The severe compression in the shock layer in front of the vehicle and subsequent, rapid expansion into the wake are characterized by high temperature, thermo-chemical nonequilibrium processes. Implicit algorithms required for efficient, stable computation of the governing equations involving disparate time scales of convection, diffusion, chemical reactions, and thermal relaxation are discussed. Robust point-implicit strategies are utilized in the initialization phase; less robust but more efficient line-implicit strategies are applied in the endgame. Applications to ballutes (balloon-like decelerators) in the atmospheres of Venus, Mars, Titan, Saturn, and Neptune and a Mars Sample Return Orbiter (MSRO) are featured. Examples are discussed where time-accurate simulation is required to achieve a steady-state solution.

Nomenclature

a	sound speed
A_m	$\dfrac{\partial \bar{f}_m}{\partial \bar{q}_m} \sigma_m$
$\mathcal{a}_L$	$\dfrac{\partial \bar{r}_L}{\partial \bar{q}_{L-1}}$, Eq. (5a)
B_m	$-\dfrac{\partial \bar{h}_m}{\partial \Delta \bar{q}} \dfrac{\partial \Delta \bar{q}}{\partial \bar{q}_L} \sigma_m$
$\mathcal{B}_L$	$\dfrac{\partial \bar{r}_L}{\partial \bar{q}_L}$, Eq. (1)
c_1, c_2	inviscid and viscous relaxation factors, respectively
$C_{v,tr}$	translational-rotational mode heat capacity at constant volume
$C_{v,V}$	vibrational-electronic mode heat capacity at constant volume
$\mathcal{C}_L$	$\dfrac{\partial \bar{r}_L}{\partial \bar{q}_{L+1}}$, Eq. (5b)
D	diameter
e	energy per unit mass
e_V	vibrational-electronic energy per unit mass
E	total energy per unit mass
$\bar{f}$	inviscid flux vector
$\bar{h}$	viscous flux vector
H	total enthalpy
L	cell index or reference length
M	Mach number
$\mathcal{M}$	mixture molecular weight
$\mathcal{M}_i$	molecular weight of species i
$\mathcal{M}_L$	inviscid flux part of $\mathcal{B}_L$, Eq. (2)
$\mathcal{N}_L$	viscous flux part of $\mathcal{B}_L$, Eq. (3)
p	pressure, N/m^2
$\bar{q}$	dependent variable vector
q_w	wall heat transfer rate, W/cm^2
$\bar{r}_L$	residual vector at cell L
$\mathcal{R}$	universal gas constant
Re	$\rho_\infty V_\infty L / \mu_\infty$, Reynolds number
S_L	source term part of $\mathcal{B}_L$
T	translational-rotational temperature, K
T_V	vibrational-electronic temperature, K
u_α	velocity component α direction, α=x, y, or z
V_∞	free stream velocity
x, y, z	Cartesian coordinates

[†] Senior Research Engineer, Aerothermodynamics Branch, Associate Fellow AIAA

χ_i	mole fraction of species i
ε	eigenvalue limiting factor, $0 < \varepsilon \leq 0.3$
λ	eigenvalue
μ	viscosity
ρ	density
σ	cell wall area
Ω	cell volume

Subscripts

i	species index
m	cell wall index
w	wall surface conditions
∞	free stream conditions

Introduction

Aeroassisted planetary entry uses atmospheric drag to decelerate spacecraft from super-orbital to orbital or sub-orbital velocities. The vehicles encounter flow domains from free-molecular to continuum[1]. The severe compression in the shock layer in front of the vehicle and subsequent, rapid expansion into the wake are characterized by high temperature, thermo-chemical nonequilibrium processes. The chemical state of atmospheric constituents crossing the bow shock varies from frozen to nonequilibrium (ionization, dissociation) to equilibrium. The thermal state of internal energy modes (electronic, vibrational, rotational) varies similarly. Convective heating rates are strongly influenced by the catalytic properties of the surface and diffusion rate of atoms to the wall.

Numerical simulations are the primary source for defining environments and vehicle response to environments required in the design of planetary entry vehicles. The simulations are verified when possible with ground-based and flight test data that cover some subset of the entry corridor parameter space. Implicit algorithms are required for efficient, stable computation of the governing equations involving the disparate time scales of convection, diffusion, chemical reactions, and thermal relaxation. Point- and line-implicit treatments provide opportunities for single level storage relaxation at the expense of time accuracy. The essence of a point-implicit method is to treat all contributions to the residual from the cell center at the advanced time level – upwind formulations enable this structure by introducing cell center dependence from the convective terms. Implicit lines running across the viscous layer, solved by block tri-diagonal relaxation, utilize the same Jacobian blocks from the point-implicit formulation in the center diagonal but provide enhanced convergence.

This paper reviews these implicit algorithms as applied in the Langley Aerothermodynamic Upwind Relaxation Algorithm (LAURA)[2] to a variety of challenging (from perspective of physical and geometric complexity) problems in aeroassist simulation. It defines performance benchmarks for a model problem so that other algorithms may be compared and more efficient simulation tools may evolve. Finally, it notes examples of a commonly applied, local-time stepping (constant Courant number) procedure which precludes attainment of a steady state solution in some cases where a steady state exists.

Algorithm

Point-Implicit Relaxation:

The Langley Aerothermodynamic Upwind Relaxation Algorithm (LAURA) employs two relaxation modes: point-implicit and line-implicit. The point-implicit mode[2,3] implicitly solves only contributions of dependent variables at cell L, $\overline{q}_L$, to the residual at cell L, $\overline{r}_L$; contributions from dependent variables at neighbor cells are treated explicitly. The contributions of inviscid, viscous, and source terms are included in the point-implicit matrix, $\mathscr{B}_L$ as follows:

$$\mathscr{B}_L = S_L \Omega_L + c_1 \mathscr{M}_L + c_2 \mathscr{N}_L \qquad (1)$$

where S_L is the Jacobian of the chemical and thermal source term components of the residual, $\mathscr{M}_L$ is the Jacobian of the inviscid terms, and $\mathscr{N}_L$ is the Jacobian of the viscous terms – all with respect to $\overline{q}_L$. Scalar constants $c_1 > 1.5$ and $c_2 > 0.5$ are relaxation factors. Typical values are $c_1 = 3$ and $c_2 = 1$. Relaxation factors on the source term Jacobian have never been required.

Within the context of flux difference splitting (FDS) and Roe's averaging[4] the inviscid Jacobian is defined:

$$\mathscr{M}_L = \frac{1}{2} \sum_m |A_m| \sigma_m \qquad (2)$$

where m is summed over all faces of cell L, A_m is the Roe's averaged flux Jacobian at face m, and $|A_m|$ is defined using the absolute values of the eigenvalues of A_m. The elements of A_m are required in the definition of the FDS formulation of the inviscid flux; consequently, it is economical to reuse these

American Institute of Aeronautics and Astronautics

quantities in the formulation of the Jacobian. The absolute value of the eigenvalues may be limited from below using a variation of Harten's entropy fix[5,3]. This limiter serves to enhance stability of the relaxation algorithm and prevent formation of expansion shocks across sonic lines or carbuncles in the stagnation region. The limiter is defined such that it is neither too large – adversely effecting computed surface heating rates and shear forces, nor too small – adversely effecting stability. In the direction tangent to the boundary layer it is limited by $\varepsilon|\lambda_{max}|$; normal to the boundary layer it is limited by

$$\varepsilon \cdot max\left[\sqrt{u^2 + v^2 + w^2}, \ 0.0001 \cdot a\right].$$

The viscous Jacobian is defined:

$$\mathcal{N}_L = \sum_m B_m \sigma_m \qquad (3)$$

where B_m is the Jacobian of viscous terms across the mth face of cell L. It implicitly treats only the divided difference across the cell face. Transport properties at cell face m are linear averages of adjacent cell center values. Velocities in the shear work term are the Roe averaged quantities already computed for the inviscid flux function. Eigenvalues of B_m are positive or zero.

The change in dependent variables after a single, point-implicit relaxation step is computed as follows:

$$\left[\frac{\Omega_L}{\Delta t_L} I + \mathcal{B}_L\right]\Delta\bar{q}_L = \bar{r}_L \qquad (4)$$

where I - the identity matrix, Ω_L - the volume, and Δt_L - the time step at cell L (usually derived from a constant Courant number specification) are associated with the time derivative term of the conservation equations. LAURA generally uses a Courant number of one million (a philosophical constraint to admit only algorithms that will solve a steady equation system without dependence on time step); consequently, this term may be neglected relative to $\mathcal{B}_L$. In cases with crudely defined initial conditions or with difficult transients stability is maintained by temporarily increasing the relaxation factors c_1 and c_2. Values of 10 are usually sufficient; values up to 100 have been required on some highly energetic, multi-species aeroassist simulations.

The point-implicit option in LAURA is generally robust – though certainly not a black box. It works well in conjunction with a one-dimensional grid adaptation algorithm in LAURA that makes large-scale adjustments of the inflow boundary to align with evolving bow shock location. It

accommodates a very simple, self-contained initialization procedure for a generic family of spacecraft geometries that generates grids in a thin layer normal to the surface and allows the grid to grow out as the solution evolves. It easily handles multi-block, asynchronous relaxation. The only numerical "knobs" to control the relaxation process are the magnitudes of the relaxation factors c_1 and c_2, the frequency of Jacobian updates, and the frequency of grid re-alignments.

Line-Implicit Relaxation:

The point-implicit option is not efficient for relaxing the viscous layers. Some efficiency can be recovered by using multitasking with majority of cycles in the boundary layer or by using an over-relaxation factor $1>c_2>0.5$. However, a better approach is to introduce implicit dependence of the solution across the entire shock layer.

The line-implicit relaxation algorithm is a simple extension of the point-implicit algorithm. However, approximations to $\mathcal{A}_L$, the Jacobian of $\bar{r}_L$ with respect to $\bar{q}_{L-1}$, and $\mathcal{C}_L$, the Jacobian of $\bar{r}_L$ with respect to $\bar{q}_{L+1}$, are introduced to preserve symmetry of form with $\mathcal{B}_L$ that also improves convergence. They are defined:

$$\mathcal{A}_L = \left[\begin{matrix} -\dfrac{c_1}{2}\left(\left|A_{L-1/2}\right| + A_{L-1/2}\right) \\ - c_2 B_{L-1/2} \end{matrix}\right]\sigma_{L-1/2} \qquad (5a)$$

$$\mathcal{C}_L = \left[\begin{matrix} -\dfrac{c_1}{2}\left(\left|A_{L+1/2}\right| - A_{L+1/2}\right) \\ - c_2 B_{L+1/2} \end{matrix}\right]\sigma_{L+1/2} \qquad (5b)$$

It is assumed that sequential indices L define a continuous series of cells spanning some portion of the computational domain. The subscripts $L \pm 1/2$ refer to Roe averaged conditions on face m between cell centers L and $L \pm 1$, respectively. A more exact linearization of the residual would lead to use of $A_{L\pm1}$ in place of $A_{L\pm1/2}$ in the second occurrence of Eqs. 5; however, the present formulation provides exact cancellation of convective, downwind implicit influences and exhibits more robust convergence characteristics, particularly in the vicinity of strong shock waves at large Courant numbers.

In the present work, the source term requires no off-diagonal, implicit contribution. The line-implicit relaxation in Eq. (6) requires approximately 2.8 times more CPU time per iteration as the point-implicit algorithm in the applications described here but convergence rate more than makes up for this overhead. It requires additional storage for the off-diagonal blocks.

American Institute of Aeronautics and Astronautics

$$
\begin{bmatrix}
\mathcal{B}_{\mathrm{L}} & \mathcal{C}_{\mathrm{L}} & 0 & 0 & 0 \\
\mathcal{a}_{\mathrm{L+1}} & \mathcal{B}_{\mathrm{L+1}} & \mathcal{C}_{\mathrm{L+1}} & 0 & 0 \\
0 & \ddots & \ddots & \ddots & 0 \\
0 & 0 & \mathcal{a}_{\mathrm{L+N-1}} & \mathcal{B}_{\mathrm{L+N-1}} & \mathcal{C}_{\mathrm{L+N-1}} \\
0 & 0 & 0 & \mathcal{a}_{\mathrm{L+N}} & \mathcal{B}_{\mathrm{L+N}}
\end{bmatrix}
$$

$$
\bullet
\begin{bmatrix}
\Delta\overline{q}_{\mathrm{L}} \\
\Delta\overline{q}_{\mathrm{L+1}} \\
\vdots \\
\Delta\overline{q}_{\mathrm{L+N-1}} \\
\Delta\overline{q}_{\mathrm{L+N}}
\end{bmatrix}
=
\begin{bmatrix}
\overline{r}_{\mathrm{L}} \\
\overline{r}_{\mathrm{L+1}} \\
\vdots \\
\overline{r}_{\mathrm{L+N-1}} \\
\overline{r}_{\mathrm{L+N}}
\end{bmatrix}
\tag{6}
$$

Implicit Boundary Conditions:

Implicit treatment of boundary conditions is required to obtain good convergence with line relaxation. Boundary conditions in the present formulation are implemented with ghost cells. If the off-diagonal Jacobian at the ghost cell for L=1 is $\mathcal{a}_0$ then $\mathcal{B}_1$ is augmented by $\mathcal{a}_0 \mathcal{W}_0^{-1} \mathcal{W}_1$ where

$$
\mathcal{W}_0 d\overline{q}_0 = \mathcal{W}_1 d\overline{q}_1 \tag{7}
$$

is an expression of the dependence of the ghost cell on the boundary cell. In like manner, $\mathcal{B}_N$ is augmented by $\mathcal{C}_{N+1} \mathcal{W}_{N+1}^{-1} \mathcal{W}_N$ where $\mathcal{W}_{N+1} d\overline{q}_{N+1} = \mathcal{W}_N d\overline{q}_N$. The only non-trivial boundary condition considered here (see Appendix A) is at solid walls that account for finite catalysis and radiative equilibrium wall temperatures.

Time Accuracy:

The LAURA algorithm, in its default mode, uses single level storage and relaxes the steady form of the governing equations with a Courant number of 10^6. However, some applications considered here require time-accurate relaxation. Time accuracy (first-order in Δt) can be recovered by using constant time step advancement at all cells and by employing two levels of storage with sub-iterations to converge the current iterate before advancing to the next time level[6].

$$
\left[\frac{\Omega_{\mathrm{L}}}{\Delta t_{\mathrm{L}}} I + \mathcal{B}_{\mathrm{L}} \right] \Delta\overline{q}_{\mathrm{L}}^{k+1} = \overline{r}_{\mathrm{L}}^{k,k+1} \tag{8}
$$

The modified algorithm is conceptually represented by Eq. (8), identical to Eq. (4) except that sub-iterations on Δq^k are accommodated. Equation (6) is modified in a similar manner. The superscript (k, k+1) signifies that the latest available iterate on $\overline{q}^n + \Delta q^k$ is utilized in the evaluation of $\overline{r}_{\mathrm{L}}$. In

theory, Eq. (8) is iterated on all cells until $\Delta\overline{q}^{k+1} - \Delta\overline{q}^k$ is converged to order Δt^2. In practice $\overline{q}^{n+1}$ is updated after 10 to 20 sub-iterations on $\Delta\overline{q}$.

Algorithm Metrics:

In most applications with crude initializations the point-implicit algorithm is more robust and efficient in reducing the residual in the early stages. In fact, the line-implicit algorithm will usually fail (increase the residuals and introduce wild fluctuations) when engaged too early in the relaxation process. However, once the solution begins to converge, indicated by a three order of magnitude decrease in the error norm, the line-implicit algorithm is more efficient in terms of iteration count and CPU time. For example, Figures 1-4 show the convergence history for a benchmark problem, flow over a sphere at $V_\infty = 5$ km/s, $\rho_\infty = .001$ kg/m^3, T_∞=200K, and T_w=500K. The convergence history is plotted as a function of iteration count in Fig. 1 and as a function of CPU time in Fig. 2 for a perfect gas model on a coarse grid of 30x32 starting from a uniform flow. The grid is not adapted. CPU times are on an SGI R10000.
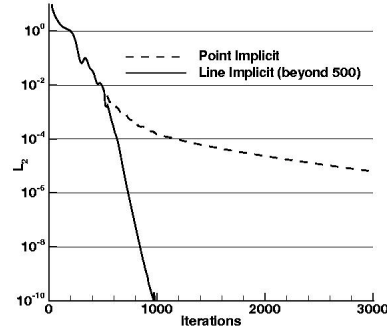

Figure 1 Comparison of point- and line implicit iteration count for sphere benchmark case with coarse grid and perfect gas model.

Subsequent grid refinements initialized from the previous coarse grid solution to 128 cells in the body normal direction gives the convergence shown in Fig. 3. Convergence rate slows significantly for the point-implicit case once the inviscid field is nearly converged but the viscous layer is not fully converged. The line-relaxation across the shock layer converges rapidly until round-off errors inhibit further error norm reduction.

Inclusion of thermochemical nonequilibrium source terms in the gas model does not significantly change the character of convergence for the benchmark case on a grid of 30x64 initialized with

free stream conditions as shown in Figure 4. In this case a 7-species model for air and a fully catalytic wall boundary condition are specified. More frequent updates of the Jacobians early in the relaxation process are required because of the rapid evolution of the solution.
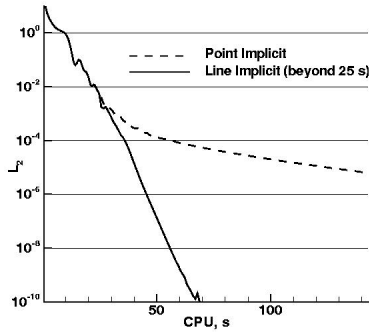

Figure 2 Comparison of point- and line implicit CPU time for coarse grid, perfect gas, sphere benchmark.
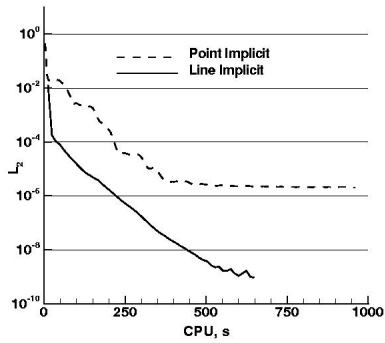

Figure 3 Comparison of point- and line implicit CPU time for fine grid, perfect gas, sphere benchmark.
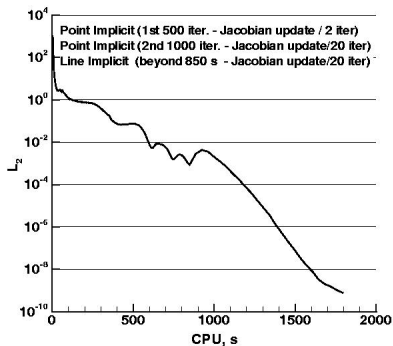
Figure 4 Typical application of point- and line-implicit algorithm showing CPU time for thermochemical nonequilibrium sphere benchmark case.

Applications

Ballutes - Spheres and Toroids:

Large, inflatable ballutes (balloon-parachutes) have been proposed[7,8] as hypersonic decelerators for planetary aerocapture applications. Table 1 defines benchmark conditions for towed spherical and toroidal ballutes. The primary configuration considered here is a towed toroid, in which the flow disturbed by the towing spacecraft passes through the hole of the toroid. The toroid is still impacted by hypersonic flow off the tow cables, which are nearly in a free molecular flow regime. Interference effects are not included in the present calculations.

Physical models in LAURA[9] have been updated to include chemical species expected in the shock layer of ballutes entering the atmospheres of Venus, Saturn, Titan, and Neptune – in addition to the models for Mars and Earth already present. The current model can accommodate 32 species and 57 reaction pairs. Examples for Mars and Venus follow.

The axisymmetric flow past a toroid at Mars for $V_\infty = 5160$ m/s and $\rho_\infty = 3.6 \ 10^{-7}$ kg/m^3 (not part of Table 1) is presented in Fig. 5. The diameter of the toroid, measured from center to center of the circular area of revolution, is 15m. The cross-sectional diameter of the circle is 2.5 m. The figure shows vibrational-electronic temperatures in a symmetry plane. The computational domain includes the flow axis, co-incident with the axis of the toroid, the inflow boundary ahead of the captured bow shock, and the supersonic outflow boundary. The flow is computed with 120 cells around the toroid, and 64 cells from the body to the outer boundaries noted above. The near wake is included to investigate the bow shock interaction along the flow axis and to accommodate future studies of flow interaction from the towing payload passing through the hole. A relatively high temperature interaction region is evident behind a Mach reflection as the intersecting bow shocks converge on the axis.

The toroid for a Venus Sample Return mission is larger than required for the Mars Microsat mission noted previously. It has a more severe entry environment as detailed in Table 1 but the larger radius reduces heating rate, even with a fully catalytic wall boundary condition. The radiative equilibrium wall temperature for this case is 712 K. The peak shock layer vibrational-electronic temperature is approximately 12000 K.

Table 1 – Ballute Simulations

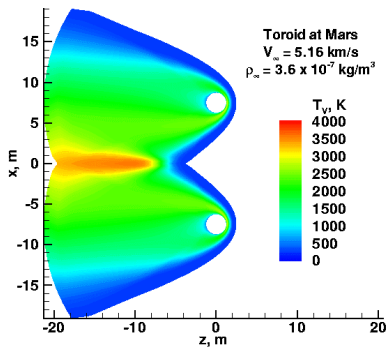| Mission	Venus Sample Return	Mars Microsat	Saturn Ring Observer	Titan Organics Explorer	Neptune Orbiter
Atmosphere, $\chi_{i,\infty}$	$CO_2 = .965$ $N_2 = .035$	$CO_2 = .953$ $N_2 = .027$ $Ar = .016$ $O_2 = .004$	$H_2 = .963$ $He = .037$	$N_2 = .983$ $CH_4 = .017$	$H_2 = .80$ $He = .19$ $CH_4 = .001$
Sphere, D, m	135.	12.	120.	48.	100.
V_∞, km/s	10.6	5.54	24.1	8.53	26.7
ρ_∞, kg/m^3	$2.2\ 10^{-7}$	$1.\ 10^{-6}$	$3.1\ 10^{-8}$	$3.0\ 10^{-7}$	$1.5\ 10^{-8}$
C_D	0.913	0.99	0.98	0.981	1.05
$\dot{q}_{max}$, W/cm^2	1.07	1.82	2.72	1.93	2.60
T_{max}, K	677.	774.	855.	785.	845.
Toroid, m Ring D / X-sec D	150. / 30.	15. / 3.	120. / 30.	52. / 13.	100. / 25.
V_∞, km/s	10.6	5.49	23.9	8.55	26.8
ρ_∞, kg/m^3	$1.6\ 10^{-7}$	$7.1\ 10^{-7}$	$2.3\ 10^{-8}$	$1.9\ 10^{-7}$	$8.2\ 10^{-9}$
C_D	1.31	1.45	1.38	1.39	1.51
$\dot{q}_{max}$, W/cm^2	1.31	1.91	2.85	2.05	2.84
T_{max}, K	712.	783.	865.	796.	864.

Figure 5 Vibrational-electronic temperature contours over toroid showing high temperature core behind shock-shock interaction in near wake.

Profiles of species mole fraction across the shock layer are presented in Figs. 6 and 7. On this scale body, shock standoff distances on the order of several meters are computed. Significant ionization (20%) is also present. Note that there is no region of chemical equilibrium; the mole fraction of CO_2, for example, does not begin significant dissociation until about 2 m in front of the body and shows a local minimum with no plateau near the boundary-layer edge. The catalysis model used here forces recombination to free stream levels at the wall; consequently effects of diffusion and recombination contribute to the rapid increase in CO_2 mole fraction from about 0.7 meters to the wall. This case was computed with the line-implicit relaxation algorithm.
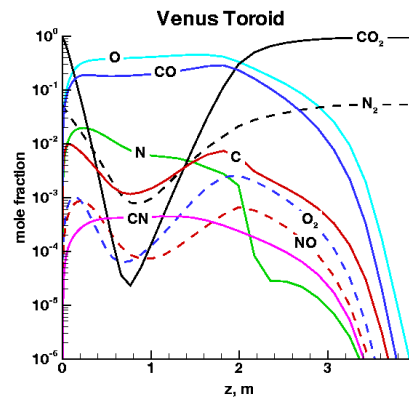

Figure 6 Mole fraction of neutrals across shock layer of Venus toroid.

Ballutes – Experimental Data:
Experimental conditions[10,11] for shot 2018 in the T5 Hypervelocity Shock Tunnel with test gas CO_2, $V_\infty = 3.714$ km/s, $\rho_\infty = 1.61\ 10^{-3}$ kg/m^3, and $T_\infty = 1570$K involving flow over a stainless steel toroid at $\alpha = 0$ was simulated with LAURA. Free stream dissociation levels were independently computed[9] to be (0.32, 0.17, 0.42, 0.09) by mole fraction for (CO_2, O_2, CO, and O) respectively. Initial comparisons of the experimental and computational results for convective heating in a CO_2 dominant atmosphere over a ballute are presented in Figure 8.

American Institute of Aeronautics and Astronautics

The effects of uncertainties in boundary conditions on predicted heating levels were not investigated. However, similar quality comparisons were obtained for shots 2013 and 2019, spanning a post shock Reynolds number range from 6.6 10^4 to 2.0 10^5.
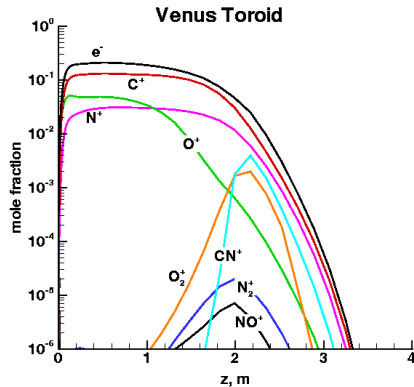

Venus Toroid

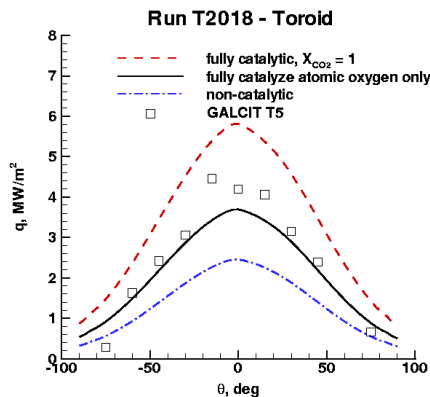Figure 7 Mole fractions of ions and electrons across shock layer of Venus toroid.

Run T2018 - Toroid

- - - fully catalytic, X_{CO_2} = 1
—— fully catalyze atomic oxygen only
-·-·- non-catalytic
□ GALCIT T5

Figure 8 Heat transfer over toroidal ballute measured in GALCIT T5 hypervelocity shock tunnel in CO_2 and computed by LAURA.

Thermal nonequilibrium is assumed and the vibrational-electronic temperature in the free stream is set equal to the translational-rotational temperature. A constant wall temperature equal to 300 K is specified. Boundary conditions for surface catalysis are varied in order to scope their influence on heating. In the fully catalytic boundary condition, the mass fraction of CO_2 is set equal to 1 at the cold wall. Mole fraction gradients are set to zero at the wall for the non-catalytic condition. In an intermediate approximation, it is assumed that atomic oxygen diffusing to the wall recombines to form molecular oxygen but a zero gradient is employed for all other species. Reasonably good agreement in heating is obtained with the boundary condition in

which only oxygen catalysis is accommodated. In all three simulated shots, the experimental data (except near $\theta = 90^o$) is bounded by the fully catalytic and oxygen only catalytic curves.

Effects of Time Accurate Simulation:

Disk and parachute-like configurations were also simulated in the early phases of this study but were not brought forward in Table 1 because of concerns regarding flow stability and aerodynamic stability. The chute configurations failed to converge using the constant Courant number relaxation scheme. Rather, they showed a periodic growth and collapse of the shock wave, the extremes of which are shown in Figure 9 for a simple Mach 6, perfect gas flow. Instabilities have been reported previously in blunt body flows with cavities[12]. While the magnitude of these chute instabilities was larger than previously reported, their occurrence was not all that surprising.
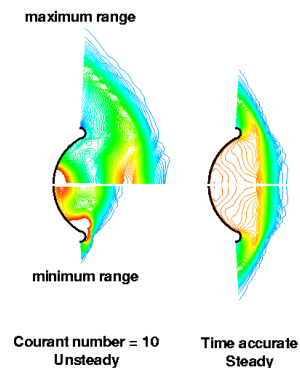

Figure 9 Density contours over chute at Mach 6 showing unsteady range of motion using constant Courant number simulation and steady solution from time-accurate simulation.

The phenomenon was interesting enough to revisit in order to generate a time accurate simulation once the capability was developed in LAURA. However, the time-accurate simulation shows the periodic motion decays to a steady state in approximately 8 cycles starting from t = 0. The time step was set at 5.23 10^{-6} s. The reference flow time, D / V_∞, is 1.05 10^{-4} s. If the constant Courant number simulation is initiated from a fully converged steady state, the steady state is retained. If the constant Courant number simulation is initiated from a "nearly-converged" time accurate solution – one that has seen a 4-order magnitude drop in error norm – the large scale periodic motion returns. Density contours across the shock front in Figure 9 are somewhat jagged because the grid had to be large

enough to fully contain unsteady motion and grid lines did not align well with the moving shock front.

This unexpected result in which the ability to achieve a steady state requires temporal accuracy has not been observed previously in typical, convex blunt body geometries. However, in a recent hypersonic code validation study[13], simulated flow over a sharp, double cone (25° / 55°) at Mach 9.5 and Reynolds number 264000 m^{-1} in nitrogen showed large scale, periodic shedding of vortices in the separation region around the 30° compression. A 1st order accurate, constant Courant number, simulation showed a steady flow for this same case. A 2nd order simulation at a lower Reynolds number (144000 m^{-1}) showed a steady flow result on the same grid. Experimental data[14] in the Calspan – University at Buffalo Research Center (CUBRC) Large Energy National Shock (LENS) tunnel for this case (Run 24) from thin-film heat transfer gauges indicated that the flow achieved steady state in the test time. The non-linear minmod flux limiter in LAURA was a suspected source of numerical ringing within the recirculation region that triggered the unsteadiness.
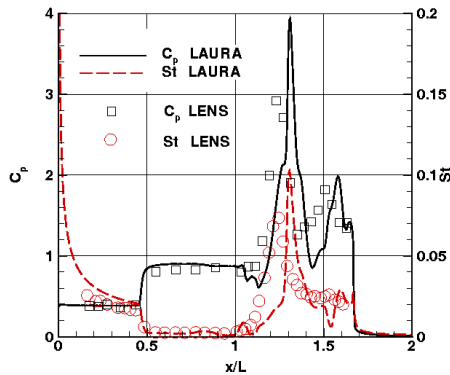

Figure 10 Pressure and heating over sharp, double cone for Run 24 of Reference 10 using time-accurate simulation to attain steady state.

In light of these recent results showing that attainment of a steady state can depend on temporal accuracy in some circumstances, the sharp, double-cone case was revisited using time-accurate simulation. The time step was set at 3.65 10^{-7} s. The reference flow time, L / V_∞, is 7.08 10^{-5} s. The flow converged to a nearly steady state – very slight oscillation of streamlines persisted in the recirculation region, but these oscillations were orders of magnitude less severe than observed in the constant Courant number simulation. Comparisons with experimental data for pressure and heating are presented in Figure 10. Good agreement with the

onset of separation is observed. Fair agreement with reflected wave peak pressure and heating location is obtained. The broad, flat pressure plateau in the recirculation region for 0.5<x/L<1 had significant, varying structure in the previous, constant Courant number simulation.

Both the chute and double-cone cases have a subsonic region contained in a concavity (rays perpendicular to the surface converge in a subsonic domain) driven by an external supersonic flow. In the typical grid that is highly stretched from the body a constant Courant number simulation means that physical time advances more rapidly away from the body than in close to the body. Perturbations associated with each relaxation step may tend to aggregate near the wall in the concavity before exiting a supersonic outflow boundary. Waves accumulate (in this non-physical temporal map), strengthen, and reflect back in to the subsonic domain in a self-sustaining but non-physical manner. This scenario is consistent with observed behavior in the two systems tested here. Certainly, not all subsonic domains with concavities induce this pseudo-unsteady behavior in constant Courant number simulations – there are many examples of compression corners with separated flow being computed with constant Courant number relaxation. It is simply noted that such flow conditions may be susceptible to pseudo-unsteady behavior in single storage level, constant Courant number relaxation and the overhead associated with implicit, time-accurate simulation may be recovered with better convergence.

MSRO – Flight at Mars:

The Mars Sample Return Orbiter is designed to use aeroassist to enter Mars orbit. Though Mars mission architectures have been revised, the MSRO mission investigated here called for the French designed orbiter to carry the US designed Earth Entry Vehicle (EEV) to Mars orbit. It would rendezvous with samples gathered in previous missions and launched from the surface to orbit. The samples would be sealed in the EEV that separates from the MSRO and returns to Earth.

One of the concerns in the design is the requirement to protect the payload from impingement heating during the aeropass. Impingement may result from the shear layer separating from the aft edge of the aerobrake and turning significantly inboard. The shear layer turning angle has been estimated from previous computational and experimental studies[15] of the Aeroassist Flight Experiment (AFE) vehicle from which MSRO design evolved. An angle-of-attack, α, of -4° corresponds to a 21° angle-of-attack relative to the base plane. At this relative angle of

8

attack the shear-layer turning angle relative to a backward facing normal to the base plane should lie between 30° and 40° (see Figure 11 of Reference 15). The payload is positioned in a region where shear layer impingement may be expected on the aft, windside corner. (Payload volume and trim angle-of-attack sensitivity to center-of-gravity constrain ability to completely avoid impingement.) Ground-based experimental and computational studies confirm shear-layer impingement on the aft corner of the cylindrical payload.

Figures 11-13 show the computed, near wake results for the MSRO at 115 seconds into the aeropass at Mars. Flow conditions are V_∞ = 5223 m/s and ρ_∞ = 2.933 10^{-4} kg/m^3 at α = -4 deg. This angle of attack provides the strongest impingement within the constraints of the guidance system. The computational grid in the plane of symmetry is shown in Fig. 11. Four hundred and thirty four simply connected, structured blocks are used in the near wake simulation. Inflow conditions were taken from a previously converged forebody solution.
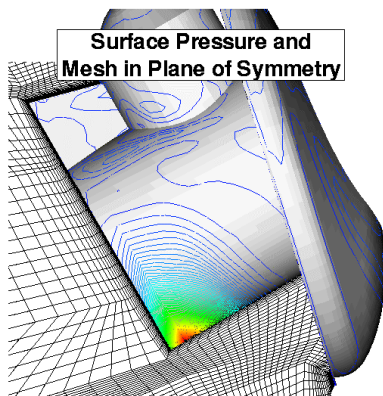

Figure 11 MSRO near wake mesh and surface pressure distribution.

The aerobrake is removed in Figure 12 to reveal the recirculation region behind the cove. Density contours in this figure clearly show the shock set up over the aft corner of the payload where impingement occurs. Figure 13 shows a heating trace along the symmetry plane of the payload, superimposed on a global view of surface heating contours. Locally high impingement heating is consistent with observations in ground–based tests. Cell Reynolds number metrics at the wall are of order 1 or less so that boundary-layer resolution should be adequate. However, the grid between the aft corner of the aerobrake and the aft corner of the cylinder (Figure 11) is not well aligned to resolve the free

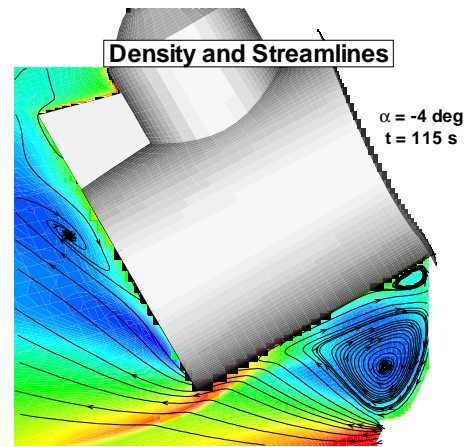shear layer so that some numerical diffusion of the flow feeding the impingement is expected.

Figure 12 Density contours and streamlines in symmetry plane featuring primary and secondary vortices behind cove of brake (removed for clarity).
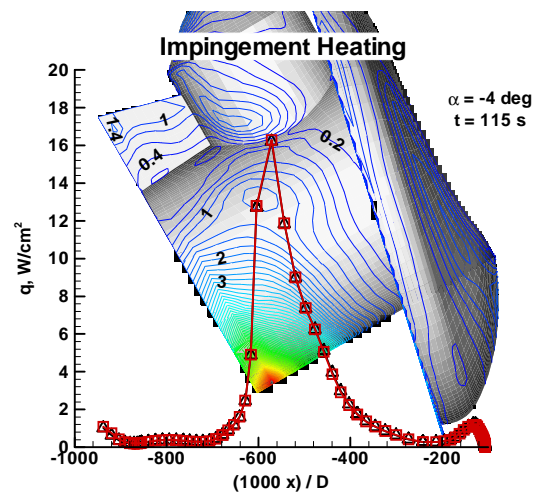

Figure 13 Trace of heating on symmetry plane of payload showing maximum value at impingement and local maximum under secondary vortex in cove region. Heating contours are on aftside of aerobrake.

MSRO – CF$_4$ tunnel:

Wind tunnel tests of the MSRO configuration were executed in the Langley CF$_4$ tunnel in order to study impingement heating levels in a gas with a relatively low ratio of specific heat – as will be encountered in flight[16]. The configuration is a scale model of the flight vehicle simulated above but a new grid (Figure 14) was generated for this study to simplify blocking topology (70 simply connected blocks) and enable automatic grid

American Institute of Aeronautics and Astronautics

adaptation into the far field. The new grid has finer resolution in the free shear layer but is still not well aligned with streamlines approaching the aft corner.
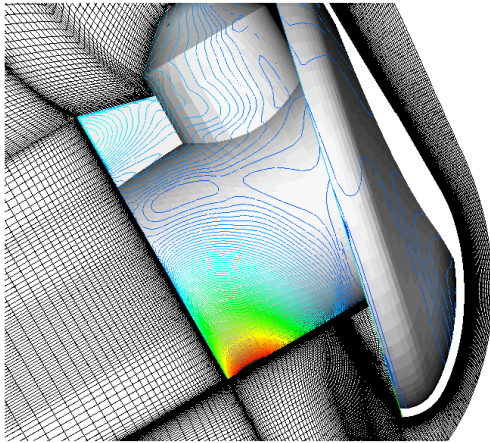

Figure 14 Grid over MSRO for CF_4 wind tunnel study with surface pressure distribution.

Simulated flow conditions are: $V_\infty = 907.4$ m/s, $\rho_\infty = 1.53 \times 10^{-3}$ kg/m^3, and $T_\infty = 201.1$K. Fully laminar flow is expected at this condition based on observed trends in the experiment as a function of Reynolds number[15]. Heating along the leading edge of the cylindrical payload (Figure 15) is non-dimensionalized by a reference stagnation point heating level defined by the method of Fay and Ridell. This reference heating is about 10% larger then measured stagnation point heating for a related case – only a few forebody measurements were made because the study was focused on payload heating issues. Comparisons between experiment (thermophosphor technique) and computation were generally within 8% on the forebody in this related case. The abscissa of Figure 15 refers to the running length along the cylinder non-dimensionalized by aerobrake reference diameter, originating at the aft corner and running forward towards the aerobrake.

The experimental data (symbols) indicate a glancing impingement, in which heating is highest at the corner. The LAURA results indicate a stronger impingement, in which a plateau level of heating is predicted, and a subsequent heating spike at the corner ($x/D = 0$) where there is a rapid thinning of the boundary layer as flow expands into the wake. A grid refinement (factor 2 in the streamwise and circumferential directions) provides better resolution of the shear layer but shows essentially no change (less than 3%) in surface heating. A heating spike near $x/D=0.3$ is grid induced – 4 blocks fan out from this location to define the cove region and the "streamwise" coordinate of the two central blocks in

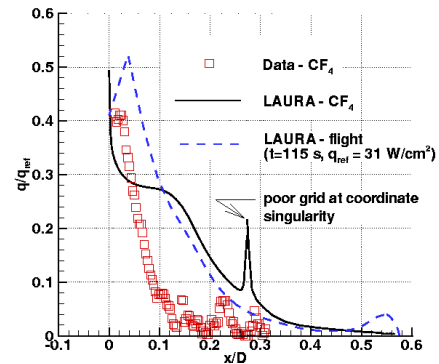the fan spans the boundary layer with inadequate resolution.

Figure 15 Impingement zone heating on cylinder along plane of symmetry.

The flight simulation of heating from Figure 13 is rescaled and plotted in Figure 15. In this case, q_{ref} is the computed heating level at the stagnation point on the forebody. At an earlier point in the trajectory (t=70s – not plotted here) the same trend is observed but it scales lower such that the maximum value is $q/q_{ref}=0.3$. The grid along the cylinder was coarser in the flight case but did not have a singularity. There is no plateau in heating – possibly because the grid is too coarse to support one. Still, the general trend is that LAURA predicts a larger area of high heating surrounding impingement on the given grids than measured in CF_4. Additional simulations are planned with re-aligned grids and, possibly, application of slip boundary conditions in attempt to resolve differences in the CF_4 case.

Concluding Remarks

Point- and line-implicit relaxation algorithms within Program LAURA for aeroassist applications are defined. The strategy of opening with a more robust point-implicit solver and closing with a more aggressive and efficient line relaxation was applied to every problem in this paper. Convergence metrics are documented for a model problem. Implicit wall boundary conditions for the fully coupled, thermochemical nonequilibrium system are required to make the line relaxation strategy work. These conditions are defined herein.

Hypersonic flows with subsonic regions bounded by a local concavity were observed to support periodic, unsteady behavior using a constant Courant number relaxation but recovered a steady flow behavior using time-accurate simulation. The behavior is thought to emerge from the temporal

mapping allowing accumulated perturbations to reflect back into the subsonic domain.

Hypersonic flows over spherical, toroidal, and concave ballute (balloon-parachute) decelerators for planetary missions are tested to demonstrate applications with diverse chemical and thermal models in severe environments. Representative environments for entries to Venus, Mars, Saturn, Titan, and Neptune are documented. A parachute-like ballute exhibited the "unsteady" behavior noted above. Comparisons to experimental heating data in T5 for hypersonic flow over a toroid in CO_2 show heating levels bounded by two strongly catalytic models for recombination at the surface.

Simulation of flow over a Mars Sample Return Orbiter adds geometric complexity to the suite of tests. The focus here is on the magnitude of heating on the payload behind an aerobrake caused by impingement of energetic flow expanding around the corner of the aerobrake. Simulations at a representative flight condition and in a CF_4 tunnel are compared to thermophosphor heating data surrounding the location of shear-layer impingement on the payload. There is a somewhat stronger turning of the shear layer toward the payload in the CFD simulation than evident in the wind tunnel data; however, both sources show roughly the same level of peak heating at the aft corner of the payload.

Acknowledgements

Appendix A – Implicit Boundary Conditions

The differential expressions for temperature, pressure, and mole fraction as functions of $d\overline{q}$ in the context of the two-temperature model are:

$$dT = \frac{1}{\rho C_{v,tr}} \left[\left(\frac{u_\alpha^2}{2} + e_v - e \right) d\rho - u_\alpha d\rho u_\alpha + d\rho E - d\rho e_v \right] \quad (A1)$$

$$dT_V = \frac{1}{\rho C_{v,v}} \left[-e_v d\rho + d\rho e_v \right] \quad (A2)$$

$$dp = \frac{\mathscr{R}T}{\mathscr{M}_i} d\rho_i + \frac{\mathscr{R}T_V}{\mathscr{M}_e} d\rho_e$$
$$+ \frac{\mathscr{R}\rho}{\mathscr{M}} \left[(1 - \chi_e)dT + \chi_e dT_V \right] \quad (A3)$$

$$d\chi_i = \frac{\mathscr{M}}{\rho \mathscr{M}_i} [d\rho_i - \chi_i \frac{\mathscr{M}_i}{\mathscr{M}_j} d\rho_j] \quad (A4)$$

Equations (A1) and (A2) are substituted into Equation (A3) to express dp as a function of $d\overline{q}$ alone, where $d\overline{q} = [d\rho_i, d\rho u_\alpha, d\rho E, d\rho e_v]$. Equation (A3) accounts for electron pressure that is a function of T_V in the two-temperature model; consequently, the sum over species i in the first term of Equation (A3) does not include electrons because they are accounted in the second term. Equation (A4) involves a sum over index j for each mole fraction i. Each occurrence of $d\rho$ involves an implied sum over $d\rho_i$.

The implicit treatment of the boundary conditions on temperature uses the differential expressions $dT_0 = 0, dT_{V,0} = 0$, derived from a specification of constant wall temperature in the ghost cell. The coefficients of each differential element of $d\overline{q}$ for these relations fill the rows associated with conservation of total energy and vibrational electronic energy in $\mathcal{W}_0$ of Equation (7). This formulation is used for both constant wall and radiative equilibrium wall temperature boundary conditions, ignoring the dependence of the temperature on heat transfer rate in the latter case.

The boundary condition for zero pressure gradient in differential form is $dp_0 = dp_1$. The coefficients of each differential element of $d\overline{q}$ in Equation (A3) fill the row associated with maximum species density in $\mathcal{W}_0$ and $\mathcal{W}_1$, respectively. The boundary condition on species mole fraction χ_i for the general case of finite surface catalysis is a function of gradients of χ_j. For the spectrum of fully catalytic to finite catalytic boundary conditions the condition $d\chi_{i,0} = 0$ is imposed at the ghost cell for all species conservation laws except for the one noted above where the pressure boundary condition was substituted. In the case of a non-catalytic wall a zero gradient in mole fraction is imposed such that $d\chi_{i,0} = d\chi_{i,1}$. Finally, the no slip condition is imposed with $d\rho u_{\alpha,0} = -d\rho u_{\alpha,1}$.

Convergence of the non-catalytic case using line relaxation is slower than the fully catalytic case. The error norm still drops faster than the rate achieved by the point-implicit method but the line-

implicit method abruptly diverges just as a fully converged state appears to be at hand. This behavior is observed even when the implicit treatment of mole fraction in the ghost cell uses the fully catalytic approximation – the demise just takes longer. Such behavior is indicative of a singularity in the coefficient matrix associated with the converged, non-catalytic state but this conjecture has not yet been confirmed analytically.

References

[1] Gnoffo, Peter A.: "Planetary-Entry Gas Dynamics," Ann. Rev. Fluid Mech. 1999, 31:459-94.

[2] Gnoffo, Peter. A.: "An Upwind-Biased, Point-Implicit Relaxation Algorithm for Viscous Compressible Perfect Gas Flows," NASA TP 2953, February 1990.

[3] Cheatwood, F. M. and Gnoffo, P. A.: "User's Manual for the Langley Aerothermodynamic Upwind Relaxation Algorithm (LAURA)", NASA TM 4674, April 1996.

[4] Roe, P. L.: "Approximate Riemann Solvers, Parameter Vectors, and Difference Schemes", *J. Comput. Phys.,* vol. 43, no. 2, Oct. 1981, pp. 357-372.

[5] Harten, Ami: "High Resolution Schemes for Hypersonic Conservation Laws", *J. Comput. Phys.,* vol. 49, no. 2, Feb. 1983, pp. 357-393.

[6] Mitterer, K. F.; Mitcheltree, R. A.; and Gnoffo, P. A.: "Application of Program LAURA to Perfect Gas Shock Tube Flows – A Parametric Study", NASA TM 104190, January 1992.

[7] Hall, J. L.: "A Review of Ballute Technology for Planetary Aerocapture", Presented at the 4th IAA Conference on Low Cost Planetary Missions, Laurel, MD, May 2-5, 2000.

[8] Hall, Jeffery L.; and Le, Andrew K.: "Aerocapture Trajectories for Spacecraft with Large Towed Ballutes," Paper AAS 01-235, Feb 2001

[9] Gnoffo, Peter A.; Gupta, Roop N.: and Shinn, Judy L.: "Conservation Equations and Physical models for Hypersonic Air Flows in Thermal and Chemical Nonequilibrium," NASA TP-2867, 1989.

[10] Rasheed, A; Fujii, K.; Valiferdowsi, B.; and Hornung, H.: "Preliminary Experimental Investigation of the Flow over a Toroidal Ballute," GALCIT Report FM 00-4, July 7,2000.

[11] Rasheed, A.; Fujii, K.; Hornung, H. G.; and Hall, J. L.: "Experimental Investigation of the Flow Over a Toroidal Aerocapture Ballute," AIAA 2001-2460, June 2001.

[12] Huebner, L. D. and Utreja, L. R.: "Mach 10 Bow-Shock Behavior of a Forward-Facing Nose Cavity," JSR, Vol. 30, No. 3, pp291-297, May-June 1993.

[13] Gnoffo, P. A.: "CFD Validation Studies for Hypersonic Flow Prediction," AIAA 2001-1025, Jan. 2001.

[14] Holden, M. S. and Wadhams, T. P.: "Code Validation Study of Laminar Shock/Boundary Layer and Shock/Shock Interactions in Hypersonic Flow Part A: Experimental Measurements," AIAA 2001-1031, Jan. 2001.

[15] Gnoffo, P. A.; Price, J. M., and Braun, R. D.: "Computation of Near-Wake Aerobrake Flowfields", *JSR,* Vol. 29, No. 2, March-April 1992, pp182-189.

[16] Horvath, T. J., Heiner, N. C., Olguin D. M., Gnoffo, P. A., and Cheatwood, F.M. "Afterbody Heating Characteristics of a Proposed Mars Sample Return Orbiter," AIAA-2001-3068, June, 2001.

American Institute of Aeronautics and Astronautics